

Electrocapillary drop actuation and fingering instability in a planar Hele-Shaw cell

Thomas Ward and Matthew Walrath

Department of Aerospace Engineering, Iowa State University, Ames, Iowa 50011-2271, USA

(Received 5 September 2014; revised manuscript received 18 December 2014; published 26 January 2015)

The electrically driven displacement of a viscous poorly conducting Newtonian fluid drop positioned between conducting parallel plates is studied both theoretically and experimentally. A mathematical expression for the average-steady velocity is developed by using Darcy flow analysis with an interface pressure that includes a contribution from Maxwell stresses at the advancing gas-liquid boundary. Experiments were performed using silicone oil at plate separation distances less than the capillary length for voltages ranging 250–750 V resulting in a change in velocity of approximately one order of magnitude. This suggested that the driving force was proportional to the square of the applied voltage, a feature that is common among fluid motion driven by electrical phenomena. The trailing interface revealed a disturbance for large fluid displacements that is analogous to a fingering instability. The channel widths were small such that we could predict the transition from a single finger that grows linearly to a single finger that grows exponentially and to multiple fingers that grow exponentially, all occurring within the range of voltages studied. The theory and experiments show good agreement with classic interfacial linear stability analysis.

DOI: [10.1103/PhysRevE.91.013012](https://doi.org/10.1103/PhysRevE.91.013012)

PACS number(s): 47.15.gp, 47.55.nb, 47.56.+r, 47.61.Fg

I. INTRODUCTION

In this paper we investigate an efficient method to transport a liquid drop over a relatively short distance in a two-dimensional Hele-Shaw cell channel. The immediate attractiveness of this actuation method will impact fields where liquid transport in confined geometries driven by means requiring no moving parts is desirable. The technique utilizes electric-Maxwell stresses generated along the interface of a nonaqueous dielectric liquid [1–3]. Poorly conducting fluids such as oils, which tend to wet most surfaces, are examples of dielectric liquids. Electrically driven actuation of an oil is not generated by the pressure gradient resulting from a change in local interface curvature that is typically associated with electrowetting on dielectric (EWOD) surfaces [4–8]. Instead, dielectrophoretic (DEP) forces generate a net *normal* component of the Maxwell stress. The net normal stress produces an effect at the gas-liquid interface that is similar to a capillary pressure or an *electrocapillary pressure* [9]. Furthermore, low power consumption is guaranteed when actuating poorly conducting fluids. This is a direct result of oils being very poor conductors with electrical conductivities that are approximately five to seven orders of magnitude smaller than most aqueous liquids. So a small but finite current will yield a large value for the voltage, ϕ_0 , and subsequently even larger values for the electric field, the square of which is used to calculate values for the Maxwell stress [10–14]. Furthermore, all analyses for the utilization of DEP for liquid actuation result in velocities that are independent of the plate separation distance [9,15]. This is a direct result of the electrocapillary pressure being proportional to the inverse of the square of the plate separation distance. Also consider that most oils possess excellent thermal stability allowing them to operate under high temperature conditions. This guarantees their stability against evaporation and also opens up the possibility of utilizing drop actuation in confined geometries for the purpose of heat transfer [16].

Many recent developments in regard to liquid actuation though have centered on developing devices based on the electrowetting phenomenon, or more precisely electrowetting on a dielectric (EWOD) surface [17–19]. But most of these studies are performed by the utilization of thin-solid dielectric coatings on the electrode surfaces in order to reduce the harmful effects of the relatively large electrical currents [$O(1\text{ mA})$ for EWOD versus $O(1\ \mu\text{A})$ for DEP] that are required when drop actuation is generated by electrowetting [4–8]. Furthermore, the dielectric layer is hydrophobic causing aqueous liquids to have larger contact angles than they would on a bare-metal electrode surface. Neither transport method is a new topic and both have a literature dating back to the late 1800s when Pellat [20] and Lippman [21] separately studied dielectric and electrowetting behavior. For EWOD systems determining the relationship between velocity and voltage is not easy because the moving contact line heavily influences stability [5,22,23]. This can lead to hysteric motion making bistability impossible.

The direct mathematical analysis of drop motion when governed by DEP exists because it is rather straightforward to relate bulk fluid motion to a net normal stress acting along a fluid-fluid interface. To demonstrate this fact consider a parallel-plate capacitor with gap dimension b that is much less than the liquid capillary length ℓ_c , and a channel width a that is much larger $a/\ell_c > 1$. The system is one of the many electrical analogs to a pump or gravity driven Hele-Shaw cell device [8,24–26]. For this particular system the device is partially filled with a drop of silicone oil, an amount just large enough to cover a trench etched into one of the indium-tin-oxide (ITO) electrode surfaces. The purpose of etching the trench is so that the trailing interface ($x = x_T$ initially located at $x_{T_0} = 0$) and the top electrode of the device may be grounded while the advancing interface ($x = x_N$) of the drop can be held at constant electric potential ϕ_0 (see Fig. 1). The wetting properties of the liquid and substrate are such that the contact angle and hence the largest capillary pressures γ/b are initially the same at

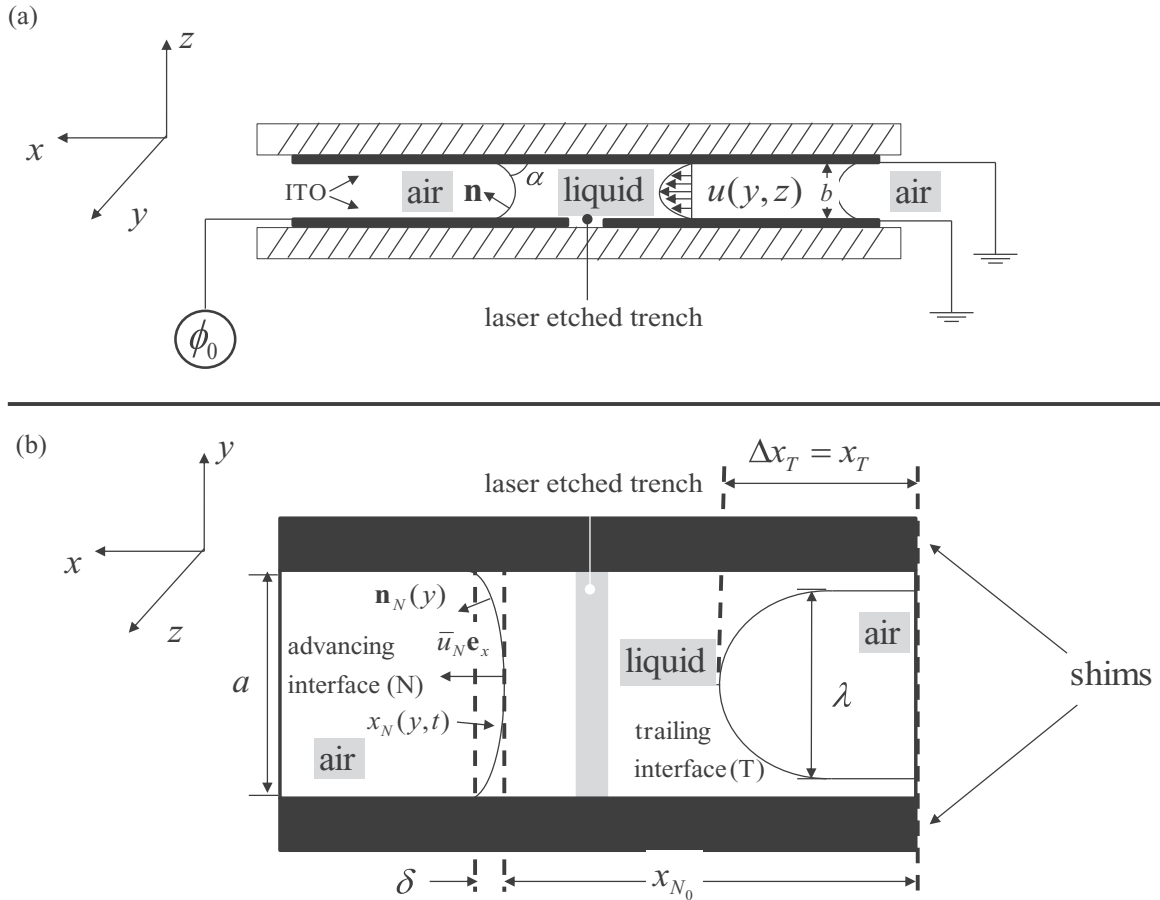


FIG. 1. (a) Side view of a horizontal parallel plate electrode Hele-Shaw cell. The substrate is glass coated with a thin layer of indium-tin-oxide (ITO) metal. A laser is used to etch a trench in the center of the bottom channel so that a separate charge may be applied to the left and bottom halves. (b) Top view of Hele-Shaw cell apparatus. Here the channel width and other relevant quantities are displayed.

the leading and trailing interfaces. Electrowetting may reduce the leading edge pressure but the surface tension (~ 15 mN/m) and contact angle $\alpha \sim 0$ are small so that any reduction in these quantities will be negligible when compared to the electrocapillary pressure [3].

The speed of the trailing interface’s finger tip for low voltage is linear and can be determined using mass conservation similar to the analysis of Fairbrother and Stubbs [27], i.e., $u_T \propto \bar{u}_N$ where u_T is the velocity at the finger’s tip. But for many of the experiments performed we observed exponential growth of the trailing interface’s finger tip position with respect to time. This justifies employing Saffman-Taylor’s linear stability analysis [28–32] to determine critical behavior in terms of the applied voltage. In the analysis here we have set the wavelength from Saffman-Taylor’s linear stability analysis equal to the measured width of the finger generated by the penetrating fluid. We justify setting the wavelength equal to the width of the finger since the wavelength according to the Saffman-Taylor analysis divided by the channel width is almost unity, $\lambda/a \sim 1$, for the range of voltage-generated velocities studied here. Therefore, within the range of experimental parameters studied exists the transition from a Fairbrother and Stubbs type analysis (trailing interface velocity determined by mass conservation) [27] to Saffman-Taylor type analysis (trailing interface velocity determined by linear stability analysis)

[28–32]. If this is correct then we can double the value of the measured wavelength and compare with the values determined from the Saffman-Taylor analysis to predict the onset of exponential growth of a *single* finger which we call the first critical voltage, $\phi_{0,\lambda/2}$. Furthermore, we are able to directly use the Saffman-Taylor analysis to predict the critical voltage for the transition to tip splitting, called the second critical voltage, $\phi_{0,\lambda}$.

Experiments were performed to test the validity of the electrocapillary approximation limit that is based on an electrohydrostatic model. The interest here was to test the hypothesis of a voltage based velocity as the operating parameter for flows driven by electrocapillary pressure. This was done by providing elapsed time versus both advancing and trailing interface positions for a range of voltages, resulting in velocities that span a decade in value. An electrocapillary linear stability analysis based on the Saffman-Taylor procedure is presented in the next section. Following this section are the experimental setup and procedure with some discussion of the results. First, the advancing interface velocity is measured and compared with theoretically predicted values. Then the trailing interface’s finger tip velocity and interface morphologies are observed and characterized as a function of the operating parameters all in the context of the Saffman-Taylor stability analysis. The experiments will be compared with the analytical

results with a discussion of possible sources for the qualitative and quantitative discrepancy between theory and experiments. Finally, some concluding remarks and future experiments are presented in the last section.

II. ELECTROCAPILLARY LINEAR STABILITY ANALYSIS

A. Electrically driven Darcy flow

Consider the geometry shown in Fig. 1 of a parallel plate electrode apparatus separated by a uniform distance b with channel width a . The channel is filled with a silicone oil drop of volume V . The liquid wets all of the channel wall surfaces. A visible wetting layer of thickness δ extends from the minimum spanwise meniscus x_{N_0} , at the region containing the side channel walls and fluid-fluid interface. The distance between the plates is much less than the capillary length, or the hydrostatic Bond number is small $\text{Bo} = (b/\ell_c)^2 \ll 1$ where $\ell_c = \sqrt{\Delta\rho g/2\gamma}$. Here ρ_L ($\rho_L \gg \rho_G$) is the liquid phase density, g is the gravitation acceleration constant, and γ is the surface tension. The relevant fluid electrical properties are the conductivity σ_G, σ_L and the electric permittivity $\epsilon_G \epsilon_0, \epsilon_L \epsilon_0$, respectively, where ϵ_0 is the permittivity of free space. Air has a conductivity that is typically assumed to be zero, $\sigma_G \approx 0$, while silicone oil has a value $\sigma_L \approx 10^{-13}$ S/m. The electrode plates consist of indium-tin-oxide (ITO) metal coated glass pieces. On the bottom plate a trench is etched along the centerline spanning the y direction by removing the metallic material with a laser until there is no electrical connection between the two halves that contain ITO. The trench depth is much smaller than the distance separating the parallel plates, while the trench width is larger than the plate separation distance b but much less than the channel width a . With this configuration it is possible to apply a positive voltage to either side of the bottom plate while grounding the other.

Silicone oil is a dielectric liquid that contains no free charges so $\nabla^2\phi = 0$, where ϕ is the electric potential [10,11]. The air-liquid interface also cannot generate free charges even in the presence of strong electric fields except during dielectric breakdown. The liquid volume is large enough such that the liquid covers the trench but does not completely fill the channel. The top plate is grounded, $\phi = 0$, along with the right half of the bottom electrode. Along the top and bottom electrodes that overlap the advancing interface of the drop, the electric potential is held constant at $\phi = \phi_0$. In the region away from the gas-liquid interface the potential varies linearly like $\phi(x) = \phi_0 z/a$, and the electric field $E = -d\phi(x)/dx = -\phi_0/a$ is uniform. The interface spanning the distance separating the plates is treated as a rigid surface that is not deformed by either the electric field or fluid motion. This allows one to determine the electric field along the interface by using electrical boundary conditions for poorly conducting fluids [3]. Then with the electric field it is possible to determine the electrical contribution to the interfacial pressure.

As the external voltage is applied to the other half of the bottom electrode the advancing interface of the liquid drop travels the distance of the unfilled portion of the channel after a certain amount of elapsed time t . Given that the span and length of the device are both much larger than b we conclude that it is sufficient to describe the liquid pressure by using

the familiar Darcy flow equations. The equation are applicable for the advancing liquid with $u_N = -\frac{b^2}{12\mu} \frac{dP_L}{dx}$. This equation can be integrated once to yield $P_L(x) = -\frac{12\mu u_N}{a} x + C_0$. The constant is set equal to the reference pressure, or $C_0 = 0$. Explicit expressions for the pressure and velocity along the advancing interface, $x = x_N$, are discussed in Appendix A. The analysis results in an expression for the average velocity of

$$\bar{u}_N = \frac{\Delta\epsilon\epsilon_0\phi_0^2}{24\mu x_{N_0}} \left[1 - \frac{\delta}{4x_{N_0}} \right], \quad (1)$$

where the wetting layer length δ (see Fig. 1) appears in the expression.

The electric Reynolds and electric capillary numbers, written in terms of the average velocity, are $\text{Re}_E = \frac{\bar{u}_N b}{\nu}$ and $\text{Ca}_E = \frac{\bar{u}_N \mu}{\gamma}$, respectively. Note that the electric capillary number [33] with $\delta/x_{N_0} \rightarrow 0$ is analogous to the electrohydrostatic Bond number. Here, we seek to predict the first and second critical voltages $\phi_{0,\lambda/2}$ and $\phi_{0,\lambda}$ corresponding to the appearance of a single finger and multiple fingers at the trailing interface, respectively, in terms of the capillary number. Expressions for these values in terms of the advancing interface velocity, physical properties, and device dimensions are developed in the next section.

B. Saffman-Taylor instability analysis: Trailing interface velocity

As mentioned in the Introduction the ability to move the drop in a high aspect ratio geometry is a highly desirable feature of the proposed liquid actuation method. But the geometry also complicates the problem of stable and bistable motion of the drop since the fluid wets the surfaces. For wetting liquids the gas phase must penetrate the channel as the trailing interface forms and expands with a concave meniscus spanning the channel, called a finger. The stability of the trailing interface has been studied in a similar context and we apply the results of those analyses for this particular problem. The goal is to determine the stability criteria in terms of applied voltage ϕ_0 that can be tested experimentally.

It should be noted that a single finger appears in the stable case but with a steady velocity that is faster than the advancing one [27,34]. The velocity of the trailing interface for this special situation can be determined according to mass conservation [27]. But that analysis is not developed in this paper since it yields a stable (linear relationship) condition. Instead we focus on developing expressions between the applied voltage, physical properties, and device dimensions for the condition where a larger voltage is applied. For larger applied voltages the trailing interface finger narrows in some cases, or splits in others, and then translates at an exponential growth rate. The critical wavelength for this to occur will be expressed in terms of the half and full wavelength values, or first and second critical voltage, respectively, as mentioned in the Introduction.

According to the Saffman-Taylor stability analysis the trailing interface velocity is determined by considering perturbation to the trailing interface of the form

$$x_T = C_\beta e^{iny + \beta_k t}. \quad (2)$$

Here $n = 2\pi/\lambda$ is the wave number, C_β is a scaling constant, and β_k is the growth rate. The variable i is an imaginary number so the equation suggests that positive values for the growth rate produce harmonic disturbance along the interface in the y direction. The channel of width b is on the order of a single finger's width. An instability of one full wavelength represents both a peak and a trough while a single finger is only a peak. Therefore we use the half, $k = \lambda/2$, and full, $k = \lambda$, wavelengths to denote the onset of the exponential growth rate for single and multiple fingers, respectively. The velocity of the trailing interface $u_T = \bar{u}_N + C_\beta \beta_k e^{iny + \beta_k t}$ is determined from continuity similar to the analysis of Fairbrother and Stubb [27] but with the perturbations to the interface described above. The stability analysis is performed by inserting the pressure from the curvature spanning the channel $\kappa_a = \frac{d^2 x_T}{dy^2}$ into the Darcy flow solution for the velocity [28,29]. Plugging in the terms for the velocity we see that $\beta = 0$ for critical wavelengths $\lambda_{\text{crit}} \leq \pi b \text{Ca}_E^{-1/2}$, i.e., there will be no exponential growth rate of the single finger that forms. For $\pi b \text{Ca}_E^{-1/2} < \lambda_{\text{crit}} < 2\pi b \text{Ca}_E^{-1/2}$ a single finger will form and grow at an exponential rate. Likewise for $\lambda_{\text{crit}} \geq 2\pi b \text{Ca}_E^{-1/2}$ the interface will grow exponentially but with multiple fingers.

The critical stability according to the Saffman-Taylor analysis leads to the critical voltages ϕ_{0_k} :

$$\frac{\pi b}{a} \left(\frac{6\gamma x_{N_0}}{\Delta\epsilon\epsilon_0 \left[1 - \frac{\delta}{4x_{N_0}}\right]} \right)^{1/2} < \phi_{0_{\lambda/2}} < \frac{2\pi b}{a} \left(\frac{6\gamma x_{N_0}}{\Delta\epsilon\epsilon_0 \left[1 - \frac{\delta}{4x_{N_0}}\right]} \right)^{1/2} \quad (3)$$

for the first critical voltage associated with the exponential growth rate of a single finger and

$$\phi_{0_\lambda} \geq \frac{2\pi b}{a} \left(\frac{6\gamma x_{N_0}}{\Delta\epsilon\epsilon_0 \left[1 - \frac{\delta}{4x_{N_0}}\right]} \right)^{1/2}, \quad (4)$$

for the second critical voltage associated with the exponential growth of multiple fingers. According to these two expressions a larger value for the wetting layer length relative to the minimum drop length δ/x_{N_0} tends to increase the critical voltages.

A dimensionless relationship between the product of the growth rate and instability wavelength $\beta\lambda$ can be written as a function of the capillary number and a term involving the plate separation distance and λ or

$$N_{\beta_{\lambda/2}} = \frac{\beta\lambda\mu}{\pi\gamma} = \text{Ca}_E - \frac{1}{12} \left(\frac{b\pi}{\lambda} \right)^2 \quad (5)$$

for the growth rate of a single finger and

$$N_{\beta_\lambda} = \frac{\beta\lambda\mu}{2\pi\gamma} = \text{Ca}_E - \frac{1}{3} \left(\frac{b\pi}{\lambda} \right)^2 \quad (6)$$

for the growth rate of a multiple ones. In the following sections experiments that were performed to test the main hypothesis for leading edge velocity, instability wavelength, and growth rate are discussed.

III. EXPERIMENTS: MATERIALS AND PROCEDURE

The parallel plate electrodes each consisted of a ($75 \times 50 \text{ mm}^2$) piece of ITO (indium-tin-oxide) coated glass (Delta Technologies). The metal coated surfaces had a roughness of $< 0.02 \mu\text{m}$ per 5-mm peak to peak distance making them extremely flat and smooth reducing the possibility of contact line effects [22]. The distance between the plates b was fixed at either 50, 100, or 150 μm using precision spacers (Accutrex) and paper clamps. Spacers were placed apart at either $a = 15$ or 30 mm for a given experimental setup. Wires for the power supply and ground connections were attached to each piece of glass using alligator clips. This apparatus was placed on a small stand with black paper in the background that helped enhance image contrast (see Fig. 2 for the setup). The electric potential was applied using a low power Spellman high-voltage unit capable of 2 kV maximum output at 0.5 mA.

Three different oil viscosities were used in the experiments: 5, 10, and 100 centistokes silicone oils or equivalently $\mu = 0.0048, 0.0096$, and 0.096 Pa s , each with density of approximately 960 kg/m^3 . The electric permittivity constant was measured previously to be $\epsilon_L = 2.9$ for the silicone oil ($\epsilon_G \approx 1$ for air) and is independent of viscosity. $\epsilon_0 = 8.854 \times 10^{-12} \text{ N V}^{-2}$ for the permittivity of free space. The surface tension was approximately 16–20 mN/m, for silicone oil on ITO based on previous studies [3]. Voltages ranged 250–750 V when possible and in 125-V increments. For the smallest plate separation distance of 50 μm it was not possible to generate dc voltages at the two highest voltage values of 625 and 750 V due to dielectric breakdown of the air that partially fills the gap. Liquid volumes were either 30 and 60 μl for the 50- μm gap, 40 and 80 μl for the 100- μm gap, or 50 and 100 μl for the 150- μm gap with 15- or 30-mm spacer separation, respectively. This translates into initial average drop length values of \bar{x}_{N_0} of 40, 26, or 22 mm.

The experimental procedure began with a thorough cleaning of the glass slides and the plastic gap spacers. The purpose was to ensure that there was no residue-fluid left on the surfaces. All pieces were then dried using compressed air. It was important not to use a cloth or towel when drying the glass since it could scratch the surface and reduce transparency or cause pinning of the liquid. Then it was necessary to identify the side of the etched piece of glass that contained the trench and to place this side up. The plastic spacers were placed perpendicular to the trench along the side of the glass slide containing the etched trench. The nonetched piece of glass, ITO side down, was then placed on top of the assembly. This was followed by careful positioning of the plastic spacers at the desired channel width to ensure that the channel was parallel. The channel width was then measured using calipers. The next step was to attach the output voltage clip to one side of the etched glass, and ground the other side and the nonetched piece of glass. Finally, fluid was added to the grounded side of the channel using a pipette. Capillary pressure due to the narrow gap moved the fluid such that it covered the etched trench. Then the high voltage unit was turned on to a prescribed voltage and the air-liquid interface position was recorded using a charge-coupled device (CCD) camera (Pixelink) at five to ten frames per second and a high resolution CCD lens (Pentax). The fluid displacement was measured by taking an average of the interface position, \bar{x}_N ,

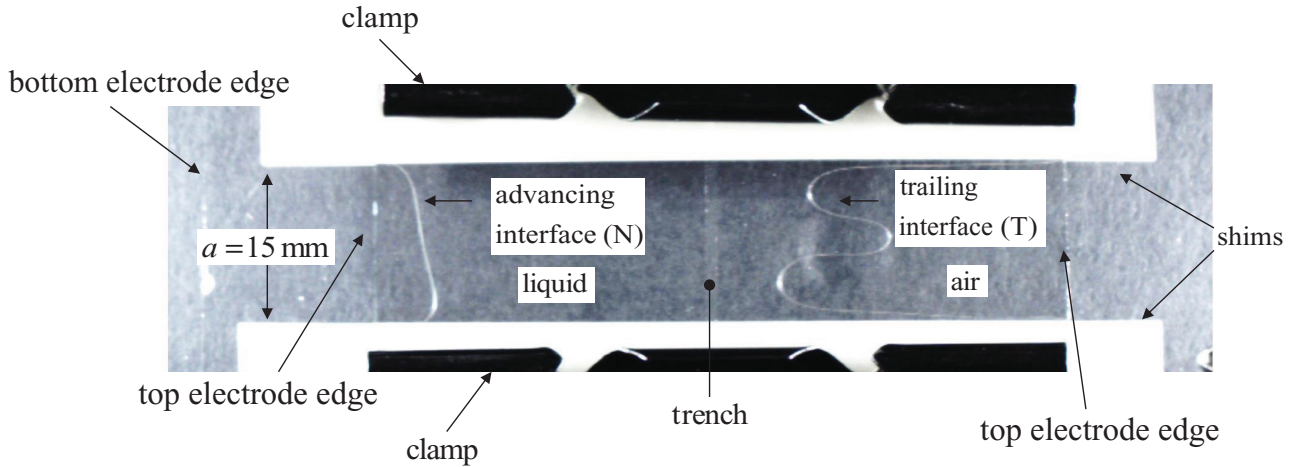


FIG. 2. (Color online) Top view of experimental setup. Image after approximately 1 s of elapsed time. The relevant parameters are $a = 15 \text{ mm}$, $b = 100 \mu\text{m}$ with $\phi_0 = 750 \text{ V}$.

from each image of a movie corresponding to an experiment. The measurements were performed using a front tracking algorithm written using MATLAB. Information for the trailing interface x_T was determined by measuring the tip of the fastest growing finger.

The range of dimensionless parameters Ca_E , Bo_a , Bo_b , and Re_E may be estimated with knowledge of the physical properties. The Bond numbers for the interface spanning the gap b were in the range $0.001 < \text{Bo}_b < 0.01$ for $b = 50\text{--}150 \mu\text{m}$ and physical parameters as listed. The Bond numbers for the interface spanning a are estimated to be $0.1 < \text{Bo}_a < 10$ using the same surface tension value. The electric Reynolds and capillary numbers were in the range $0.004 < \text{Re}_E < 15$ and $6 \times 10^{-5} < \text{Ca}_E < 0.001$, respectively. With such low capillary number we concluded that any film formation at the trailing interface was negligible [34]. Values for δ/x_{N_0} were also measured. The values were approximately 0.1–0.2 for $a = 15 \text{ mm}$ and larger, 0.25–0.4, for $a = 30 \text{ mm}$. The values did not change much with plate separation distance with no values measured for $b = 50 \mu\text{m}$ due to poor visibility. The predicted critical voltage ϕ_{0_c} for multiple fingering in the experiments with $100\text{-}\mu\text{m}$ plate separation distances are 269 and 538 V for the 30 and 15 mm channel widths, respectively. For the $150\text{-}\mu\text{m}$ plate separation distance experiments the values are larger at 371 and 742 V for the 30- and 15-mm channel widths, respectively.

IV. EXPERIMENTS: RESULTS

A. Interface and fingering instability

Figure 3 shows images of drops with 5-centistoke (cS) fluid viscosity being displaced in a 15-mm channel in Figs. 3(a)–3(f), and 100-cS fluid viscosity in a 30-mm channel distance in Figs. 3(g)–3(l). The voltages are held constant at 250 V, Figs. 3(a)–3(c), 750 V, Figs. 3(d)–3(f) and Figs. 3(j)–3(l), and 625 V, Figs. 3(g)–3(i). The parallel plate separation distance is constant at $150 \mu\text{m}$ for all experimental images in Fig. 3. Images are shown just prior to the application of the voltage potential for the 5-cS fluid. For the 100-cS fluids images are shown at a few seconds immediately after the application of the voltage potential. This is due to the fact that the higher viscosity

liquids require a greater elapsed time to travel the channel distance. So it required a few seconds to begin image capture in order to record the full displacement for each voltage. The final frame, just before the finger tip at the trailing interface reaches the trench, is shown in the right hand column of Fig. 3. Examples for the length estimates used to determine these finger widths are denoted with λ in the last column for each set of experiments.

The advancing interfaces for the two 15-mm channel gap experiments, Figs. 3(a) and 3(d), show similarities. The visual similarities in these two experiments appear until the end of the experiments shown in Figs. 3(c) and 3(f). The time scales though are very different with the higher voltage experiment reaching the final frame, Fig. 3(c), in approximately one-tenth the time required to reach the final frame in the 250-V experiment shown in Fig. 3(f). The advancing interfaces also look similar for the two 100-cS viscosity fluid experiments shown in Figs. 3(g) and 3(j). The time scale between the first and last frame are similar for these two sets of experiments. The trailing interface morphologies though do not appear to be similar. The trailing interface for the higher voltage experiment, Fig. 3(l), produces two fingers rather than the one finger shown for the lower voltage experiment in Fig. 3(i). Even though the initial trailing interfaces do not *appear* to be the same the reader should recall that image capture begins a few seconds after the voltages are applied for the higher viscosity experiments.

B. \bar{x}_N and x_T vs time

Figure 4 shows a sampling of curves for the measured average advancing interface \bar{x}_N and trailing interface x_T versus elapsed time t for the same experiments shown in the previous Fig. 3. The trailing interface finger always travels an equal or greater distance in a shorter time in each graph. Figure 4(a) shows results for the 5-cS fluid, corresponding to Figs. 3(a)–3(f). The advancing interface for the 750-V experiments travel approximately the same distance as the interface in the 250-V experiments shown in Fig. 4(a). But the time required to travel that distance is approximately ten times greater for the interfaces in the 250-V experiments, regardless of considering

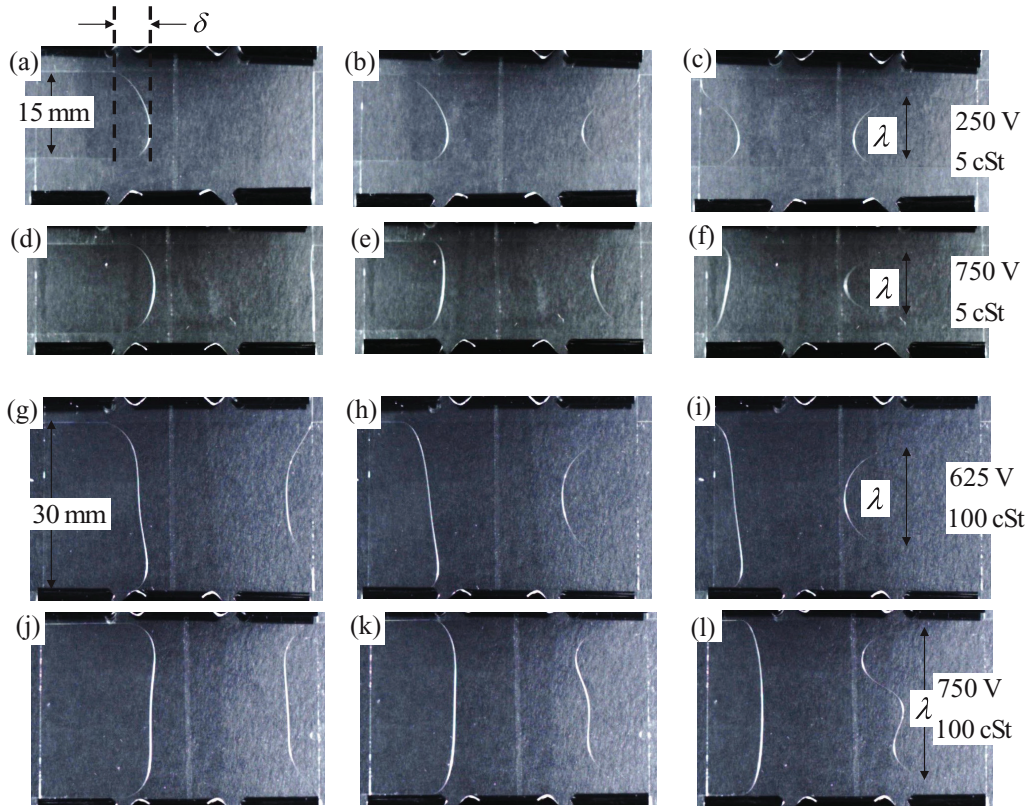


FIG. 3. (Color online) Images of liquid transport in parallel plate electrode Hele-Shaw cell device. Images (a)–(c) show images for a 5-centistoke (cS) fluid in a 15-mm channel with 250 V applied. The images are taken at times of approximately 0, 30, and 60 s respectively. Images (d)–(f) show images for a 5-cS fluid in a 15-mm channel with 750 V applied. The images are taken at times of approximately 0, 8, and 16 s respectively. Images (g)–(i) show images for a 100-cS fluid in a 30-mm channel with 625 V applied. The images are taken at times of approximately 0, 85, and 170 s respectively. Images (j)–(l) show images for a 100-cS fluid in a 30-mm channel with 750 V applied. The images are taken at times of approximately 0, 42, and 84 s respectively. The plate separation distance is 150 μm in all of the images.

the advancing or trailing interface information. The shape of each curve appears linear for both sets of experiments shown in Fig. 4(a) with slight curvature shown for the advancing interface average position versus time 250-V case. Although these curves appear linear they will be measured precisely to determine any exponential growth behavior. This is discussed further in the following sections.

Figure 4(b) shows results that are similar to those in Fig. 4(a). The difference between the two data sets is the fluid viscosity which is 100 cS in Fig. 4(b). The time scale is much larger for the higher viscosity fluids data even though the voltages are relatively large at 625 and 750 V. In these plots the difference between the shape of the curve for the advancing and trailing interfaces' positions versus time are clearly seen. For the 625-V experiments the curve for the leading edge is relatively linear compared to the curve for the trailing interface data at the same voltage. The same trend holds true for the 750-V experiments except the shape for the curve for the advancing interface appears to be slightly logarithmic.

C. \bar{u}_N and u_T vs voltage

Figure 5 shows the results for the product of the measured velocities and fluid viscosity versus the square of the applied voltage potential ϕ_0^2 . There are two figures for the advancing interface, Fig. 5(a), and trailing interface, Fig. 5(b), data. Also

plotted are solid lines for the theoretically determined velocity versus voltage values. These are plotted using the minimum and maximum values for the drop lengths $\bar{x}_{N_0} = 0.040$ and 0.022 m, respectively. We also chose a single value for the corner wetting layer length of $\delta/\bar{x}_{N_0} = 0.4$, the maximum recorded value from all of the experiments. The voltage values vary between 250 and 750 V, or by approximately an order of magnitude when squared. This is reflected in the values for the velocities which also span an order of magnitude, 0.2–2 Pa m. Also plotted are the velocities for a given voltage averaged over all the channel widths, plate separation distances, voltages, and volumes. Error bars are shown to represent the standard deviation for the averaged values. For the advancing interface data shown in Fig. 5(a) it appears that the average values fall between the two lines indicating the theoretical velocity versus voltage values. The same though is not true for the trailing interface data shown in Fig. 5(b). Here the average trailing interface data are consistently above the theoretical values, as expected. The magnitude of the standard deviation appears to increase up to 625 V where it then decreases.

D. Wavelength λ vs Ca_E

Figure 6 shows the estimates for the instability wavelength normalized by the channel width versus the electric capillary numbers based on the measured velocities. The symbols

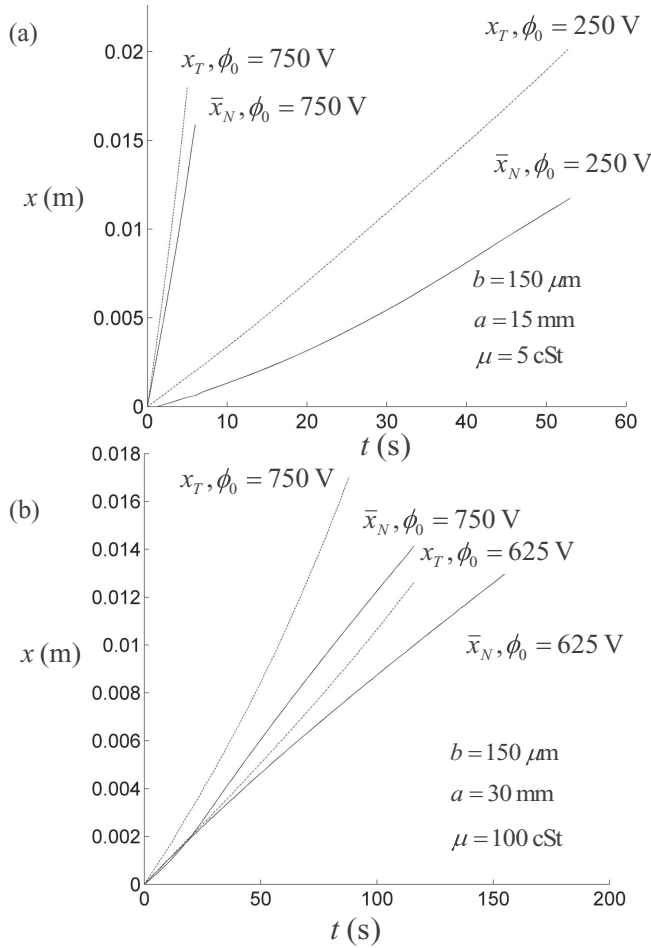


FIG. 4. Plots of leading and trailing interface displacements $\Delta\bar{x}_N$ and Δx_T vs time for same voltages, channel widths, and plate separation distance as shown in Fig. 3 with (a) 5-cS and (b) 100-cS fluid viscosities.

represent the fluid viscosity used for a particular experiment. The data are organized according to plate separation distance b and channel width a . No data are shown for the smallest plate separation distance of 50 μ m due to poor resolution of the trailing air-liquid interface. Also plotted in each graph is the predicted wavelength that leads to exponential growth (instability) as determined by Saffman-Taylor's analysis (solid line $\lambda_{\text{crit}} = \pi b \text{Ca}_E^{1/2}$) [28,29,32]. The two solid lines shown in each plot correspond to critical wavelengths associated with the full λ and half $\lambda/2$ measured values. The lines were drawn to separate regions [see Fig. 6(d)] where different trailing interface motion is observed: single finger width with no exponential growth, single finger width with exponential growth, and tip splitting of the finger with exponential growth.

The normalized measured wavelength values range from approximately 0.4–1 in each graph. The capillary numbers range $10^{-4} - 10^{-3}$, or approximately one order of magnitude. The graphs also show that the normalized measured wavelengths cross each of the predicted instability wavelength lines for some value of the capillary number. The degree of fingering (single or multiple) as determined by the graphs varies according to the channel width. For example in Figs. 6(a) and 6(c), the predicted instability wavelength occurs at

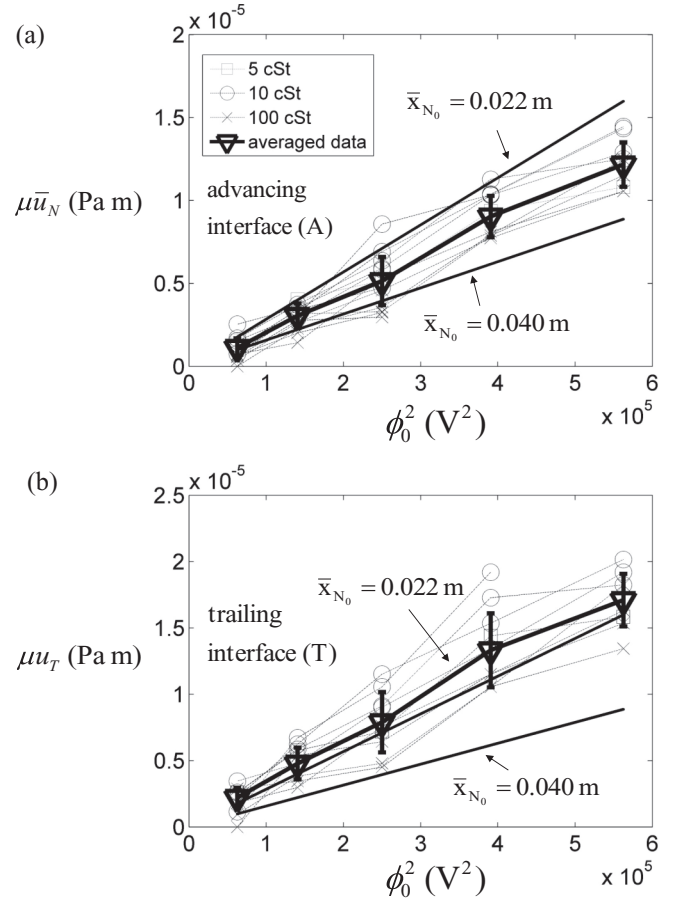


FIG. 5. Plots of the product of measured velocities and viscosities for the (a) leading $\mu\bar{u}_N$ and (b) trailing μu_T edges of the drops versus the square of the applied voltage ϕ_0^2 . The values for velocity are determined by linear fit through advancing and trailing interface displacement vs time data, respectively. Theoretical values for $\bar{x}_{N_0} = 0.022$ and 0.04 m with $\delta/x_{N_0} = 0.4$ are also plotted.

relatively large normalized wavelength values. The result is that in total only two of the measured experimental data points lie in the region where tip splitting is predicted. An image for one of these two points is shown in Fig. 2. Meanwhile a doubling of the channel width produces a richer variety of trailing interface motion and morphology as seen in Figs. 6(b) and 6(d). In Fig. 6(b) only one data point lies in the region where no exponential finger growth is predicted with similar results shown in Fig. 6(d).

E. Growth rate β analysis

The information used to produce the graphs shown in Fig. 4 can be further analyzed to produce estimates for the instability growth rates β . This is done by first estimating the velocity using a difference scheme, i.e., $u_T \approx \Delta x / \Delta t$ where Δx is the difference in measured tip location and over the time interval Δt . Since the value for the change in velocity is never zero according to Eq. (6), then the change in velocity with time Δu the velocity difference over time interval Δt can be approximated using $\Delta u \approx C_T (e^{\beta t} - 1)$ where C_T is a constant. To apply this equation to the data the initial trailing interface velocity (first nonzero value) is subtracted from the

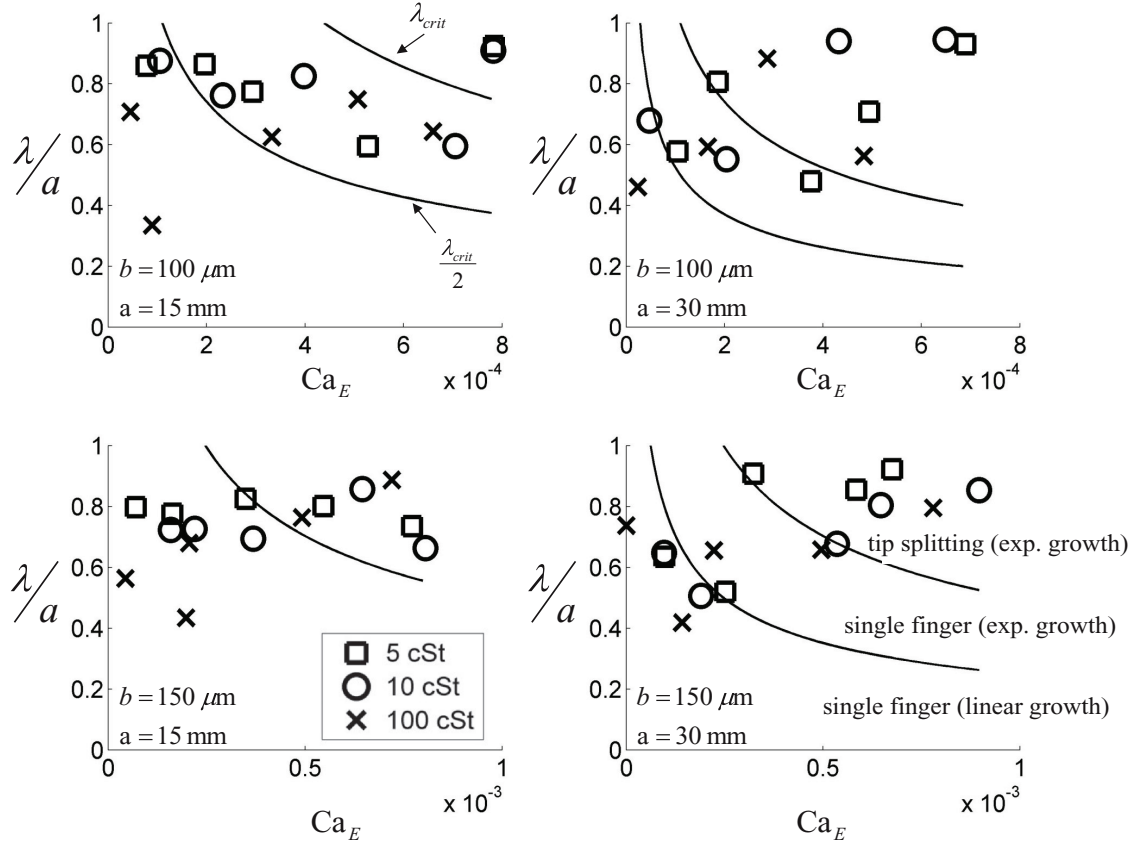


FIG. 6. Plots of the measured values for the finger wavelength normalized by the channel width λ/a vs capillary number. The solid lines are the predicted instability wavelength based on the full and half wavelengths λ_{crit} and $\lambda_{crit}/2$ determined using the Saffman-Taylor ($\lambda_{crit} = \pi b Ca_E^{1/2}$) analysis. The corresponding channel width and plate separation distances are (a) 15 mm and 100 μm , (b) 30 mm and 100 μm , (c) 15 mm and 150 μm , and (d) 30 mm and 150 μm . In (d) the regions where single finger constant, single finger exponential, and multiple finger exponential growth are denoted. The viscosities are denoted with \square 5 cS, \circ 10 cS, and \times 100 cS in each graph.

total velocity data set for a given experiment. The final velocity value $\Delta u(t_{end})$ can be matched directly to the approximate equation using $\beta = \ln |1 + \Delta \frac{u(t_{end})}{C_T}| / t_{end}$. So the only unknown parameter is the constant C_T . The value for C_T is modified to minimize the error between the curves for the measured Δu data and the values determined by the approximate equation. The same process was used in [35] to determine the area expansion rate of a gas injected into a Hele-Shaw cell at constant pressure.

Figure 7 shows the normalized growth rates versus capillary number. Each growth rate β is normalized according to Eqs. (10) and (11). The change in values for the vertical axis occurs mainly due to the product of the measured growth rate and viscosity $\beta\mu$ since the λ values lie within a narrow range and the surface tension is constant. This scaling yields a one-to-one relationship between β and the capillary number minus a term involving the square of the plate separation distance [Eqs. (10) and (11)]. There are two plots showing the results for wavelength of 2λ in Fig. 7(a) and λ in Fig. 7(b). Symbols are used to denote the fluid viscosity of 5, 10, or 100 cS. Only values for $\beta > 0$ are shown in these graphs and no 50- μm parallel plate separation distance data are shown due to the poor resolution of the trailing interfaces.

Figure 7(b) shows data utilizing the raw normalized measured λ values versus capillary number minus the additional

term. Most of the data points lie well below the dotted line denoting the one-to-one relationship between the two values. The data appear to fit the line better for smaller values of the growth rate and for the 100-cS fluids. When using twice the value of the measured wavelength 2λ the data appear to follow the one-to-one relationship more closely as shown in Fig. 7(a). Here there are several data points that lie above the line but more still lie below. Even though most of the points lie below the line there is still good agreement in the trends where most of the 5- and 100-cS data tend to increase for increasing value along the horizontal axis.

V. DISCUSSION

We should address two important assumptions used to develop expressions for the leading and trailing interface velocities. First, a thick residual film would produce an additional capillary pressure that opposes the leading edge velocity motion. The measured capillary numbers are $Ca_E < 10^{-3}$ suggesting thin residual films based on calculations using any of the relevant existing power law relationships for the steady velocities produced by the advancing interface [34]. Second, notice that even though the trailing interface increases in area (the length of the interface when viewed from above) there does not appear to be any decrease in the drag from this

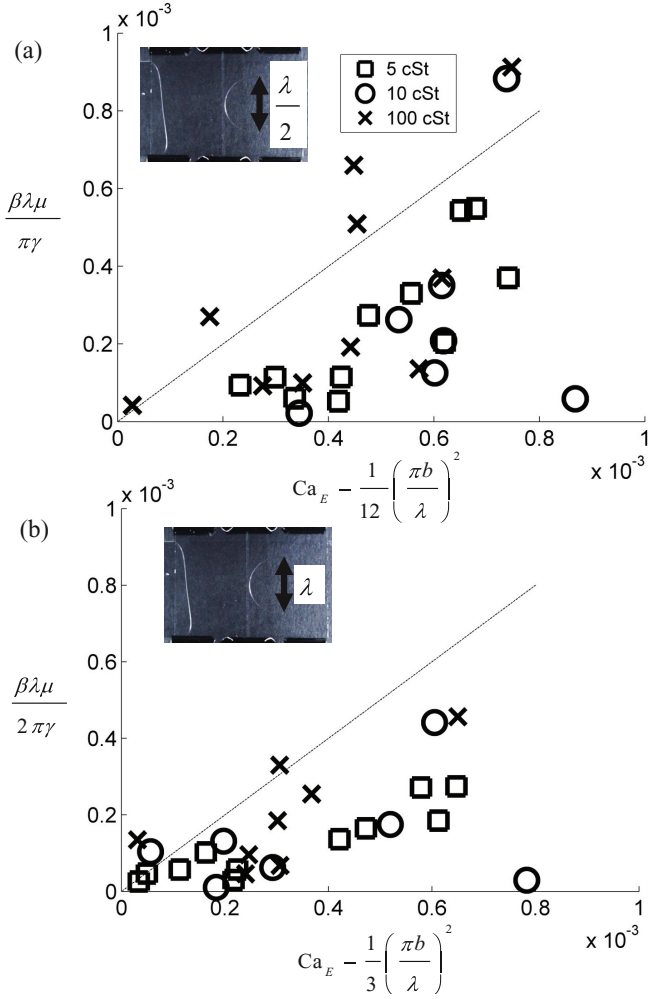


FIG. 7. (Color online) Plots of the dimensionless instability growth rate (a) $N_{\beta_{\lambda/2}}$ and (b) $N_{\beta_{\lambda}}$ vs capillary, Ca_E minus square of the dimensionless plate separation distance $(\pi b/\lambda)^2$. In (a) the value for twice the wavelength is used representing the first critical voltage while in (b) the measured instability wavelength λ is compared directly to the growth rate representing the second critical voltage.

according to the \bar{x}_N vs time plots shown in Figs. 4(g)–4(l). If the trailing edge capillary pressure were to decrease then the 625-V case [Figs. 4(g)–(i)] would have the same slightly transient velocity as the 750-V case [Figs. 4(j)–4(l)]. So the assumption of δ/a leading to negligible additional drag appears to have been correct (see Appendix A). But the analysis that has been presented does not predict the transient behavior that is observed in the plots shown in Fig. 4. These are more likely due to the small offset (deviation from parallel) in the spacers used to form the channel walls of the Hele-Shaw cell device. A brief analysis for this situation is presented in Appendix B for the case of flat advancing and trailing interfaces.

In Figs. 5(a) and 5(b) the predicted velocities agree well with the experimental data. In particular the slope of the theoretically predicted lines shown in Fig. 5 provide an upper and lower bound for the experimental data averaged at each voltage value. Recall that the value for the slopes are directly proportional to the difference in electric permittivity $\Delta\epsilon\epsilon_0$ and inversely proportional to the product $24x_{N_0}$. The fact that the

slopes agree well when using the constant of 24 is reassuring since there have been other predicted values in the literature [9]. The trailing interface velocity though does not appear to agree with the same velocity scaling used for the advancing interface [Fig. 5(b)]. This is not surprising since there is always some liquid which lines the channel walls in the x direction, i.e., a finger always forms. Therefore simple volume conservation would predict a faster moving trailing interface. But according to the data shown in Fig. 4 an exponential increase is sometimes observed for the trailing interface data.

The Saffman-Taylor linear stability analysis of the trailing interface does provide some insight into the characteristic speeds for the trailing interface. In order to utilize the linear stability analysis performed by Saffman-Taylor, data were provided in Fig. 6 for the trailing interface finger wavelength. In general wider channels (larger a) result in a greater chance of observing multiple fingers generated by tip splitting at the higher end of the range of voltages used to actuate drop motion. The analysis was extremely accurate in determining regions of λ/a versus Ca_E used for predicting the occurrence of the different types of fingering events. The visual data shown in Fig. 3 clearly confirm the computed stability limit for the 150- μm experiments with 30-mm channel widths where a value of 625 V produces a single finger while at 750 V tip splitting occurs. Unfortunately the measured growth rates, Fig. 7, did not agree well with the predictions except for the lower viscosity cases. This is probably due to the fact that the slower moving fluid provided transient velocity data with better temporal resolution. But nearly all of the capillary number and gap spacing values predicted to produce exponential growth according to Fig. 6 (38 total points with 8 close to linear boundary) were measured to have exponential growth in Fig. 7 (27 total points).

In regard to the suitability of this actuation method for reversible flow that yields bistable motion [36], one would have to successfully switch the voltages in the two halves of the device. This would then cause the leading and trailing interfaces to alternate. Clearly for the situations where the leading and trailing edge velocities are constant (below the first critical voltage) bistability would be readily achieved. But given the overall small velocities (2 mm/s at the largest voltages and lowest viscosity fluid) then it would be more desirable to operate at the largest possible voltage. But above the second critical voltage multiple fingers appear. These can lead to nonlinear fingering and thus introduce the possibility of entrainment of the gas phase into the liquid thereby reducing the efficiency of the device. So the most optimal range would be below the second critical voltage but above the first, so that a single finger forms with exponential growth. Then it should be possible to successfully switch between the two states by correctly tuning the size of the device to ensure that the trailing interface position does not exceed the trench location.

VI. CONCLUSION

The problem of the two-dimensional flow of a Newtonian poorly conducting fluid driven by electricity is presented. The solution for the interface position as a function of elapsed time in the Darcy flow limit is determined. In this problem

the geometry is a two-dimensional parallel plate capacitor with plate separation distance smaller than the capillary length. The fluid displacement and flow characteristics can be parametrized using the electric Reynolds and capillary numbers.

The velocities, used to determine the dimensionless parameters, are derived by considering the normal component of the Maxwell stress acting on one of the two-dimensional fluid interfaces. The parameters have the usual nonlinear dependence on the electric potential. But the velocity and hence the dimensionless parameters are independent of the plate separation distance. This suggests that high velocities may be achieved even in microscale geometries with this pumping method.

The experiments were performed using silicone oils of 5-, 10-, and 100-cS viscosities. Since the fluids are poorly conducting it is possible to generate large voltages (>100 V) with relatively low current ($<50 \mu\text{A}$) supplied by a high voltage unit, so the system is efficient at pumping viscous fluid using low power ($\sim 10^{-4}$ W). The leading edge position versus elapsed time almost always appeared linear; while the finger tip generated at the trailing interface showed exponential displacement for certain values of the voltage. To study this feature the typical linear stability analysis performed by Saffman-Taylor was employed. The analysis yielded an expression for the minimum critical voltage to observe exponential finger growth. Both the leading and trailing interface data were in good agreement with their respective theoretical predictions.

In the future it will be beneficial to consider even higher voltages. In order to generate higher voltages it will be necessary to consider ac rather than dc applied voltages. The effect of ac voltages on both the leading and trailing interfaces velocities and interface morphologies would be of interest. Along with considering leading edge motion under ac conditions, it may be possible to generate bistable motion by alternating the voltage for both the leading and trailing interfaces.

ACKNOWLEDGMENT

The authors would like to acknowledge C. Y. Chong for his help in analyzing a portion of the data.

APPENDIX A: ADVANCING INTERFACE VELOCITY

In this Appendix we develop the analytical expression for the advancing interface velocity. To begin we develop an expression for the electric field, and subsequently the normal component of the interfacial stress. The expression is determined by applying boundary conditions for poorly conducting fluid interfaces to the Maxwell stress equation which is included in the overall interface stress balance. The resulting expression then can be used to determine the static pressure P along the interface.

The poorly conducting fluid boundary conditions are (1) the magnitude of the tangential components to the electric field are equal along the interface $\|\mathbf{E}\| \cdot \mathbf{t} = 0$, (2) zero free charge along the interface $\epsilon_0 \|\epsilon \mathbf{E}\| \cdot \mathbf{n} = 0$, and (3) conservation of electric current $\|\sigma \mathbf{E}\| \cdot \mathbf{n} = 0$ [3]. Here $\|d\| = d_G - d_L$

denotes a jump in the variable b_i across the interface. The conditions differ from a leaky-dielectric liquid by the assumption of zero net charge accumulation along the interface.

The dimensional interface stress balance for a gas-liquid interface at $x = x_N$ in electric field is given by [3]

$$\| -P(x_N)\mathbf{I} + \boldsymbol{\tau}_E \| \cdot \mathbf{n} = \mathbf{n}(\gamma_a \kappa_a + \gamma_b \kappa_b). \quad (\text{A1})$$

For the trailing interface at $x = 0$ it is

$$\| -P(0)\mathbf{I} \| \cdot \mathbf{n} = \mathbf{n} \gamma_b \kappa_b, \quad (\text{A2})$$

which is initially uniform in the xy plane. Here the interface curvature is denoted using κ . The variable \mathbf{n} is used to denote the outward pointing normal along the gas-liquid interface in the xz plane. The subscripts for the surface tension and curvature denote the direction spanning the interface, i.e., either the plate separation distance (b) or channel width (a). The electrical component of the stress is given by the Maxwell stress relationship $\boldsymbol{\tau}_E = \epsilon \epsilon_0 (\mathbf{E}_i \mathbf{E}_i - \frac{1}{2} |\mathbf{E}_i|^2 \mathbf{I})$. We have neglected writing the viscous stress $\boldsymbol{\tau}_H$ in the interfacial stress balance. For the normal stress component this is a reasonable assumption since the fluid velocity in the Hele-Shaw cell is steady and fully developed [37]. In regard to the tangential component recall that there are no free charges in the bulk or along the interface. Therefore, there is no jump in charge displacement across the interface and the tangent component of the electric field must be conserved on either side of the interface. So we must have $\mathbf{t} \cdot \|\boldsymbol{\tau}_E\| \cdot \mathbf{n} = 0$ where \mathbf{t} is the interface tangent vector. Furthermore the divergence of the Maxwell stress is exactly zero, $\nabla \cdot \boldsymbol{\tau}_E = 0$, with no free charges in each bulk fluid [10,11,14].

Then the only stress component of concern is in the direction normal to the advancing interface which is $\mathbf{n} \cdot \|\boldsymbol{\tau}_E\| \cdot \mathbf{n} = \gamma_a \kappa_a + \gamma_b \kappa_b$. We assume a small hydrostatic Bond number for the interface spanning the gap which allows one to neglect gravitational effects at the gas-liquid interface. Then by using the Young-Laplace approximation the curvatures can be written as $\kappa_a = 2 \frac{\cos \alpha}{a}$ and $\kappa_b = 2 \frac{\cos \alpha}{b}$. This should be valid for dielectric fluid interfaces subjected to large electric fields since the Maxwell stresses yield negligible modification of the contact angle [3]. We will ignore the curvature from the interface spanning the channel in Eq. (1) since the curvatures vary inversely with their characteristic lengths where $b/a \ll 1$, and the surface tensions are of similar order, i.e., $\gamma_b \kappa_b > \gamma_a \kappa_a$. The subscripts used to denote the surface tension and curvature spanning the gap will be dropped from here on.

In regard to developing an expression for the electric field recall that air has a negligible conductivity or equivalently $\sigma_G \approx 0$. So the conservation of current across the interface suggests that there is no normal component of the electric field in the liquid phase along the interface or equivalently $\mathbf{E}_L \cdot \mathbf{n} = (\sigma_G / \sigma_L) \mathbf{E}_G \cdot \mathbf{n} \approx 0$. The normal component of the electric field on the gas phase side of the interface is also zero since $\epsilon_L \mathbf{E}_L \cdot \mathbf{n} = \epsilon_G \mathbf{E}_G \cdot \mathbf{n} \approx 0$, since there is zero net accumulation of free charges. A general result of this analysis is that the electric field is always tangent to the interface spanning the gap in the xz plane for dielectric liquids in air or $\mathbf{E}_L \cdot \mathbf{n} = \mathbf{E}_G \cdot \mathbf{n} = 0$ and $|\mathbf{E}_i| = \mathbf{E}_i \cdot \mathbf{t}$. Including the continuity of the electric field across the interface yields a

second generalization, that the electric field magnitude and direction are equal on either side of the interface or $\mathbf{E}_L = \mathbf{E}_G$.

With these simplifying approximations the total electric field (with no magnetic field) \mathbf{E} is tangent to the interface. Even though the meniscus forming the interface spanning the electrode plates is curved, the electric field there must be equal to the value in the gas phase which is $\frac{\phi_0}{b}$ [38]. Mathematically this has been shown previously by forming a closed domain that includes the top and bottom electrode walls that are held at constant potential, the meniscus interface, and the electric field in the gas phase. The electric field must be conserved around this domain according to conservation of charge [10,11]. But the potential is held constant on the top and bottom plates so the tangential components of their electric fields are locally zero. So the two portions, the interface and the constant field away from the interface, must be equivalent. Then the magnitude of the electric field along the interface is approximately

$$|E_G| = \frac{\phi_0}{b}, \quad (\text{A3})$$

where $|E_L| = |E_G|$ since $\mathbf{E}_i \cdot \mathbf{n} = 0$. The equation above suggests that the curved interface spanning the top and bottom plates has negligible effect on the electric field. This is an approximation for poorly conducting fluids [1,3] which are distinctly different from leaky-dielectric liquids where in the latter the liquid conductivity can be large enough to accumulate net charges that have been shown to produce tangential fluid motion [13,14].

The expression for the gas phase pressure along the advancing interface is then

$$P_G(x_N) = -\frac{2\gamma \cos \alpha}{b} - \frac{\Delta\epsilon\epsilon_0\phi_0^2}{2b^2} + P_L(x_N). \quad (\text{A4})$$

A similar expression that does not include the electrical term exists for the trailing interface pressure,

$$P_G(0) = -\frac{2\gamma \cos \alpha}{b} + P_L(0). \quad (\text{A5})$$

The net force in the x direction (with no external forcing, $\sum F_x = 0$) that drives fluid motion is determined by integrating the interface stress components $-\iint [P_G(x_N)\mathbf{e}_x \cdot \mathbf{n}_N - P_G(0)\mathbf{e}_x \cdot \mathbf{n}_T]dA = \sum F_x = 0$ in the flow direction over the differential area $dA = dydz$. For the trailing interface we will assume that it is initially flat or $\mathbf{n}_T = \mathbf{e}_x$. This value will certainly change with time but is impossible to predict without an expression for the advancing interface velocity. In any case we find that it is a reasonable assumption to use the initial value for the elapsed time during which the liquid was displaced.

The advancing interface shape may be approximated by an even termed power series expansion in y written as $x_N(y) = x_{N_0} + \frac{\delta}{a^2}y^2 + O(\frac{\delta^2}{a^4}) + \dots$. Then the dot product of the normal and basis vector in the flow direction is $\mathbf{e}_x \cdot \mathbf{n}_N = \frac{1}{\sqrt{1+4(\delta y/a)^2}}$. The pressure though over the nonuniform interface is independent of y so it is more convenient to replace it by an average value $\bar{P}_G(x_N) = C_p P_G(x_N)$ [39] where $C_p = \int \mathbf{e}_x \cdot \mathbf{n}_N dy/a$ is an interfacial pressure coefficient. After integrating we find that the expression for the coefficient is $C_p = \frac{a}{\delta} \ln | \frac{\delta}{a} [1 + \sqrt{1 + (a/\delta)^2}] |$ representing a reduction in the pressure due to the meniscus spanning the channel

a . Locally the advancing interface pressure is reduced by approximately 10% for $a/\delta = 1$. There is nearly no reduction for $a/\delta = 2$ which typically occurs in the experiments described here [40–42]. Furthermore, the capillary pressures for the advancing and trailing interfaces are *initially* nearly opposite and equal so we eliminate the capillary pressure terms from the force balance.

Continuing to work with the force balance we recall that the liquid phase pressures are $P_L(x_N) = -\frac{12\mu u_N}{a}x_N$ and $P_L(0) = 0$ at the advancing and trailing interfaces, respectively. After combining the remaining terms in the balance equation, we find that the expression for the leading edge velocity is $u_N = \frac{\Delta\epsilon\epsilon_0\phi_0^2}{24\mu x_N}$. The velocity varies inversely with x_N which is not uniform in the y direction. To remove the dependence we find an average velocity by integrating over the area, i.e., $\bar{u}_N = \iint u dA / \iint dA = \frac{\Delta\epsilon\epsilon_0\phi_0^2}{12\mu \sqrt{\delta x_{N_0}}} \tan^{-1} \frac{1}{2} \sqrt{\frac{\delta}{x_{N_0}}}$. It is more convenient though to expand the inverse tangent function about the corner wetting layer length δ yielding

$$\bar{u}_N = \frac{\Delta\epsilon\epsilon_0\phi_0^2}{24\mu x_{N_0}} \left[1 - \frac{\delta}{4x_{N_0}} + O(\delta^2) + \dots \right] \quad (\text{A6})$$

for the first two terms. Note that the average velocity is independent of the plate separation distance [9,15]. In general the advancing interface meniscus reduces the average velocity by a percentage that is equal to a quarter of δ/x_{N_0} from the case of a drop with a uniform x_N .

APPENDIX B: VELOCITY IN CONVERGING OR DIVERGING CHANNELS

The solution for the velocity in converging or diverging channels of a Hele-Shaw cell is developed in this appendix. Consider the image shown in Fig. 8(a) of a drop in a channel of uniform gap b and bounded at the top and bottom by spacers that are not parallel to each other or the x axis. The advancing and trailing interfaces are both assumed flat in the xy plane so that $x_N \neq f(y)$ and $x_T \neq g(y)$. Let $L = x_N - x_T$ be the length of the drop with volume V . The angles α_1 and α_2 are used to denote the top and bottom deviation in degrees, respectively, from a uniform channel width of a_0 . Then $\tan \alpha_1$ and $\tan \alpha_2$ are the slopes of the spacers relative to the horizontal forming the nonuniform channel. With a positive x direction pointing to the left then the slope for the top spacer is negative in the example shown in Fig. 8(a). The slope for the bottom piece can be rotated about the x axis for the purposes of determining the velocity. It is straightforward to integrate then sum the profiles $y_1(x) = m_1x + \frac{a_0}{2}$ and $y_2(x) = m_2x + \frac{a_0}{2}$ to determine the analytical expression for the drops area,

$$A = \frac{m_1 + m_2}{2} [x_N^2 - x_T^2] + a_0b [x_N - x_T], \quad (\text{B1})$$

where $m_1 = \tan \alpha_1$ and $m_2 = \tan \alpha_2$ are the slopes. The sum $m_1 + m_2$ determines whether or not the drop flows through a contraction ($m_1 + m_2 > 0$) or an expansion ($m_1 + m_2 < 0$).

The total volume, $V = Ab$, is

$$V = \frac{(m_1 + m_2)b}{2} [2Lx_N - L^2] + a_0bL, \quad (\text{B2})$$

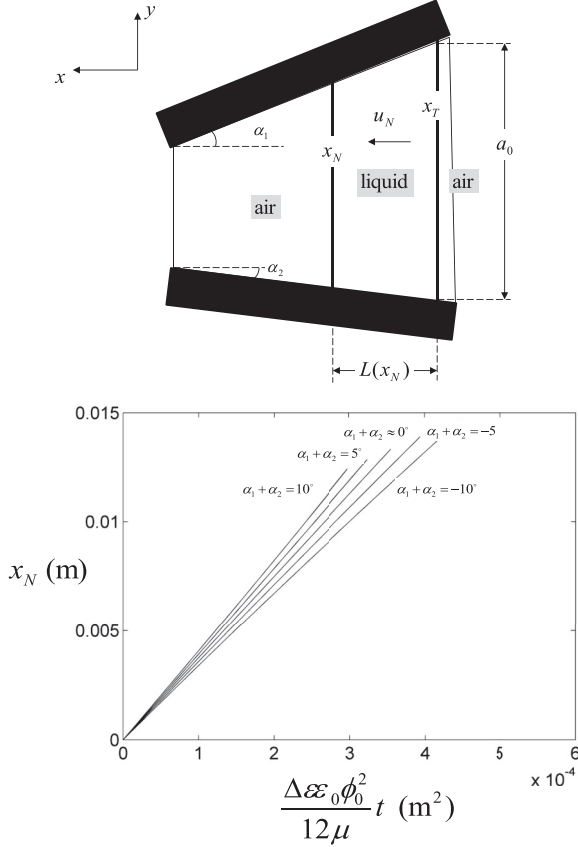


FIG. 8. (a) Schematic for system described in Appendix B. The advancing and trailing interfaces are both assumed uniform (independent of y) while the channel walls are not parallel. The angle of the top and bottom walls with respect to the horizontal are $m_1 = \tan \alpha_1$ and $m_2 = \tan \alpha_2$. (b) Results for the displacement of the advancing interface vs scaled elapsed time. The values for the channel slopes are shown in the plot.

where we have taken advantage of $x_T = x_N - L$. This expression is quadratic in terms of the length $L(x_N)$ with general solution

$$L(x_N) = \frac{1}{m_1 + m_2} [B - \sqrt{B^2 - C}], \quad (\text{B3})$$

where

$$B = x_N(m_1 + m_2) + a_0 \quad (\text{B4})$$

and

$$C = \frac{2V}{b}(m_1 + m_2). \quad (\text{B5})$$

Let $u_N = \frac{dx_N}{dt} = \frac{\Delta \epsilon \epsilon_0 \phi_0^2}{24 \mu L(x_N)}$. In order to integrate this expression we must have $B > 0$ and also $B^2 > C$. Then the expression for the elapsed time with respect to x_N after integration yields

$$t = \frac{12\mu}{\Delta \epsilon \epsilon_0 \phi_0^2} [B^2 - B\sqrt{B^2 - C} + C \ln |B + \sqrt{B^2 - C}|] - C_0. \quad (\text{B6})$$

Here

$$C_0 = \frac{12\mu}{\Delta \epsilon \epsilon_0 \phi_0^2} [B_0^2 - B_0\sqrt{B_0^2 - C} + C \ln |B_0 + \sqrt{B_0^2 - C}|], \quad (\text{B7})$$

where

$$B_0 = x_{N_0}(m_1 + m_2) + a_0 \quad (\text{B8})$$

with

$$x_{N_0} = -\frac{a_0}{m_1 + m_2} \pm \sqrt{\left(\frac{a_0}{m_1 + m_2}\right)^2 + \frac{2V}{(m_1 + m_2)b}}. \quad (\text{B9})$$

The sign for the discriminant changes depending upon whether the drop passes through a contraction or an expansion. If the sum $m_1 + m_2 > 0$ then the discriminant is added in the equation above, and subtracted if $m_1 + m_2 < 0$.

A typical plot of the results is shown in Fig. 8(b) for $m_1 + m_2$ both positive and negative. The horizontal axis is the elapsed time multiplied by the factor $\frac{\Delta \epsilon \epsilon_0 \phi_0^2}{12 \mu}$ which has dimensions of length squared per unit time.

-
- [1] T. B. Jones, *J. Appl. Phys.* **43**, 4400 (1972).
 [2] S. G. Jennings, *Phys. Educ.* **12**, 40 (1977).
 [3] T. Ward, *J. Electrostat.* **64**, 817 (2006).
 [4] S. K. Cho, H. Moon, and C.-J. Kim, *J. Microelectromech. Syst.* **12**, 70 (2003).
 [5] K.-L. Wang and T. B. Jones, *Langmuir* **21**, 4211 (2005).
 [6] D. Chatterjee, B. Hetayothin, A. R. Wheeler, D. J. King, and R. L. Garrell, *Lab Chip* **6**, 199 (2006).
 [7] D. Klarman and D. Andelman, *Langmuir* **27**, 6031 (2011).
 [8] D. Mampallil, H. Burak Eral, A. Staicu, F. Mugele, and D. van den Ende, *Phys. Rev. E* **88**, 053015 (2013).
 [9] E. S. Baird and K. Mohseni, *Nanoscale Microscale Thermophys. Eng.* **11**, 109 (2007).
 [10] J. D. Jackson, *Classical Electrodynamics*, 3rd ed. (John Wiley & Sons, New York, 1999).
 [11] D. J. Griffiths, *Introduction to Electrodynamics*, 3rd ed. (Prentice-Hall, Upper Saddle River, NJ, 1999).
 [12] D. A. Saville, *Annu. Rev. Fluid Mech.* **29**, 27 (1997).
 [13] G. I. Taylor, *Proc. R. Soc. A* **291**, 159 (1966).
 [14] J. R. Melcher and G. I. Taylor, *Annu. Rev. Fluid Mech.* **1**, 111 (1969).
 [15] T. Ward, *Langmuir* **24**, 3611 (2008).
 [16] M. Chakraborty, A. Ghosh, and S. DasGupta, *RSC Adv.* **4**, 1074 (2014).
 [17] R. A. Hayes and B. J. Feenstra, *Nature (London)* **425**, 383 (2003).
 [18] G. Beni and M. A. Tenan, *J. Appl. Phys.* **52**, 6011 (1981).

- [19] S. Chevalliot, J. Heikenfeld, L. Clapp, A. Milarcik, and S. Vilner, *J. Disp. Technol.* **7**, 649 (2011).
- [20] H. Pellat, *C. R. Seances Acad. Sci. (Paris)* **119**, 675 (1894).
- [21] G. Lippman, *Ann. Chim. Phys., cinquième série* **5**, 494 (1875).
- [22] A. L. Bertozzi and M. P. Brenner, *Phys. Fluids* **9**, 530 (1997).
- [23] H.-W. Lu, K. Glasner, A. L. Bertozzi, and C.-J. Kim, *J. Fluid Mech.* **590**, 411 (2007).
- [24] J.-H. Huh and S. Kai, *Phys. Rev. E* **68**, 042702 (2003).
- [25] T. Tóth-Katona and Á. Buka, *Phys. Rev. E* **67**, 041717 (2003).
- [26] K. Ērglis, A. Tatulcenkov, G. Kitenbergs, O. Petrichenko, F. G. Ergin, B. B. Watz, and A. Cēbers, *J. Fluid Mech.* **714**, 612 (2013).
- [27] F. Fairbrother and A. E. Stubbs, *J. Chem. Soc.* **1**, 527 (1935).
- [28] P. G. Saffman and G. I. Taylor, *Proc. R. London, Ser. A* **245**, 312 (1958).
- [29] R. L. Chuoke, P. Van Meurs, and C. Van der Poel, *Petrol. Trans. AIME* **216**, 188 (1959).
- [30] G. M. Homsy, *Annu. Rev. Fluid Mech.* **19**, 271 (1987).
- [31] C.-W. Park and G. M. Homsy, *J. Fluid Mech.* **139**, 291 (1984).
- [32] T. Maxworthy, *Phys. Rev. A* **39**, 5863 (1989).
- [33] J. C. Baygents, N. J. Rivette, and H. A. Stone, *J. Fluid Mech.* **368**, 359 (1998).
- [34] F. P. Bretherton, *J. Fluid Mech.* **10**, 166 (1961).
- [35] T. Ward and A. R. White, *Phys. Rev. E* **83**, 046316 (2011).
- [36] K. Sambath and O. A. Basaran, *AICHE J.* **60**, 1451 (2014).
- [37] F. M. White, *Viscous Fluid Flow*, 2nd ed. (McGraw-Hill, Boston, MA, 1991).
- [38] T. Ward, *J. Electrostat.* **65**, 742 (2007).
- [39] W. M. Deen, *Analysis of Transport Phenomena* (Oxford University Press, New York, NY, 1998).
- [40] P. Concus and R. Finn, *Proc. Natl. Acad. Sci. USA* **63**, 292 (1969).
- [41] P. Concus and R. Finn, *Acta Math.* **132**, 177 (1974).
- [42] H. Wong, S. Morris, and C. J. Radke, *J. Colloid Interface Sci.* **148**, 317 (1992).